

# Bragg Mirror Focusing Devices

A. D. Stoica<sup>1</sup>, M. Popovici,  
University of Missouri Research Reactor, Columbia, MO 65211, USA,

and C. R. Hubbard  
Oak Ridge National Laboratory, Oak Ridge, TN 37831, USA

## 1. Introduction

Attempts to use bent perfect crystals as neutron monochromators originate in the early seventies [1]. Understanding the focusing capabilities of crystal bending and the possibility to increase the neutron reflectivity of perfect crystals by bending [2,3] has provided a real progress of these ideas. Matrix computer codes for instrument optics design have been developed [2,4,5] to sustain the implementation of bent perfect crystals in neutron scattering.

The design of thick doubly bent perfect crystal monochromators has steadily improved [6-8], making them competitive with mosaic crystal monochromators. This is true for powder diffractometry, especially with position sensitive detection (PSD) [9,10], but also for three-axis spectrometry [11,12]. Thanks to the high transparency of silicon to thermal neutrons the perfect silicon as neutron monochromator allows using thicker crystals. However, focusing applications demand higher curvatures that cannot be reached because of the breaking limit. An alternative way is to build an effective thick crystal from thin wafers. This was first tested in the early eighties [13,14] but was implemented in the construction of monochromators only in the last years [15] as multiwafer or multilamella monochromators.

Doubly bent perfect crystal silicon monochromators were implemented in neutron stress mapping at HFIR (ORNL) and will be the choice after the reactor upgrade [16,17]. The optimal design of such a monochromator was described in a previous report [16]. Within the approach first used in these previous investigations, new imaging properties of bent crystals appear to be very promising. This report is devoted to exploring the imaging properties of bent perfect crystals. A general matrix description of diffraction on deformed perfect crystals is developed in the first chapter, which gives the results already used in the previous report for bulk and multi-wafer bent monochromators. The imaging conditions appear as a logical step following this

---

<sup>1</sup> On leave from National Institute for Materials Physics, Bucharest, Romania

approach [18] and the concept of *Bragg mirrors* as devices for non-dispersive imaging is introduced. Imaging with a thick packet of silicon wafers at the spatial resolution of a single thin wafer is demonstrated experimentally. The combination of Bragg mirrors with the time-of-flight (TOF) method is discussed. It appears to open entirely new opportunities in neutron scattering. Hopefully this will be exploited at new facilities such as the Spallation Neutron Source, now under construction in the US.

## 2. Matrix description of diffraction by deformed perfect crystals

Neutron diffraction by deformed perfect crystals can be described in the quasi-classical limit [19] in terms of geometrical optics (i.e., particle approach). The local value of the reciprocal lattice vector is defined for every point of the crystal [3]. Neutrons along a given path in the crystal are reflected with a certain probability at the points where the Bragg condition is fulfilled [20]. This is an extension of the simple "lamellar" model of diffraction advanced earlier [1]. The approach neglects the spatial extent of dynamic diffraction ( $\sim 10^{-3}$  mm) and the angular dynamic range ( $\sim 10^{-6}$  rad).

A matrix method using the corpuscular approach similar to that of Gaussian lens optics was worked out for neutron optics [21,2]. The neutron state before diffraction is specified by the spatial coordinates across the beam  $(y_0, z_0)$ , the angular deviations  $(\gamma_0, \delta_0)$  from the beam axis and the relative deviation of the wavevector  $(\Delta k_0/k)$ . The neutron state is thus defined in the five dimensional phase space by the vector  $\boldsymbol{\eta} = (y_0, k\gamma_0, \Delta k_0, z_0, k\delta_0)$ . The neutron-state after diffraction is specified in the same way by changing the subscript  $(0 \rightarrow I)$ .

In the paraxial approximation of linear relations describing the diffraction, the neutron coordinates in the horizontal (diffraction) plane are not correlated with those in the vertical plane and the wavevector deviation has no influence on the ray tracing in the vertical plane. One can thus consider separately the vectors  $\boldsymbol{\eta}_0 = (y_0, \gamma_0, \Delta k_0/k)$  and  $\boldsymbol{\eta}_I = (y_I, \gamma_I, \Delta k_I/k)$  of the neutron state in the horizontal plane and the vectors  $\boldsymbol{\zeta}_0 = (z_0, \delta_0)$  and  $\boldsymbol{\zeta}_I = (z_I, \delta_I)$  in the vertical plane. The concept of acceptance diagrams [22] is quite useful to visualize the allowed domains of these vectors - the phase space acceptance windows.

### 2.1. Thin crystal approach

A simple lens description of neutron diffraction from a thin curved crystal can be used [21]:

$$\begin{bmatrix} y_1 \\ \gamma_1 \end{bmatrix} = \begin{bmatrix} \frac{L_1 - f_1}{f_0} & \frac{L_0 L_1}{f_0} \left( 1 - \frac{f_0}{L_0} - \frac{f_1}{L_1} \right) \\ \frac{1}{f_0} & \frac{L_0}{f_0} - 1 \end{bmatrix} \times \begin{bmatrix} y_0 \\ \gamma_0 \end{bmatrix}, \quad (1)$$

where  $L_0$  is the distance to the crystal from the point where the initial state is considered,  $L_1$  is the distance from the crystal to the point where the final state is considered, and  $f_0$  and  $f_1$  are the focal lengths before and after diffraction:

$$f_0 = \frac{R_e}{2} \sin(\theta + \chi) \operatorname{sgn}(\theta + \chi); f_1 = \frac{R_e}{2} \sin(\theta - \chi) \operatorname{sgn}(\theta + \chi), \quad (2)$$

where  $R_e$  is the radius of curvature of the crystal in the horizontal (equatorial) plane, which is positive if the neutrons strike the concave side of the crystal. The factors  $\operatorname{sgn}(\theta + \chi)$  were introduced to formally allow angles to have signs (trigonometric convention). The coupling matrix in relation (1) results from a multiplication of three matrices depicting the travel of the neutron from the initial point to the crystal, the reflection by the crystal, and the travel of the neutron from the crystal to the final point:

$$\begin{bmatrix} \frac{L_1 - f_1}{f_0} & \frac{L_0 L_1}{f_0} \left( 1 - \frac{f_0}{L_0} - \frac{f_1}{L_1} \right) \\ \frac{1}{f_0} & \frac{L_0}{f_0} - 1 \end{bmatrix} = \begin{bmatrix} 1 & L_1 \\ 0 & 1 \end{bmatrix} \times \begin{bmatrix} -\frac{f_1}{f_0} & 0 \\ \frac{1}{f_0} & -1 \end{bmatrix} \times \begin{bmatrix} 1 & L_0 \\ 0 & 1 \end{bmatrix}. \quad (3)$$

By equating to zero the upper right element of the coupling matrix one gets the well-known focusing relation for lenses:

$$\frac{f_0}{L_0} + \frac{f_1}{L_1} = 1. \quad (4)$$

When relation (4) is satisfied all neutrons emerging from a point arrive to another point regardless of direction: a point is imaged by reflection into a point. The magnification  $M$  is defined as  $M = L_1/L_2$ . This definition is also valid for the image formation in the vertical plane. The matrix description of the image formation in the vertical plane is similar and within the paraxial lens optics the results are formally the same.

In the diffraction plane the wavevector is correlated with the direction through the Bragg law. For bent perfect crystals of negligible thickness one has [21]:

$$\begin{aligned}\frac{\Delta k_0}{k} &= -\cot \theta \frac{y_0}{2f_0} - \cot \theta \left( \frac{L_0}{2f_0} - 1 \right) \gamma_0 \\ \frac{\Delta k_1}{k} &= -\cot \theta \frac{y_1}{2f_1} + \cot \theta \left( \frac{L_1}{2f_1} - 1 \right) \gamma_1\end{aligned}\tag{5}$$

The wavevector deviations before and after diffraction are in fact equal, but separate notations are kept to allow for the Doppler effect or other possible inelastic phenomena.

The determinant of the reflection matrix for the thin crystal case differs from unity because the reflection is not specular from the macroscopic point of view. The asymmetric diffraction can shrink or broaden the neutron beam with the factor  $\sin(\theta-\chi)/\sin(\theta+\chi)$  but the wavevector bandwidth (introduced by the crystal thickness) undergoes a reverse transformation keeping a constant neutron phase space density.

The thin crystal approach can be extended to include nonlinear effects such as second order aberrations and curvature non-uniformity [23]. The relation (5) includes second order and third order terms to account these contributions, but in fact the wavevector deviations and the neutron reflection on a thin crystal are considered separately.

## 2.2. General solutions

From the point of view of imaging the effect of the crystal thickness consists of blurring the thin crystal ideal model of relations (1) and (5). Bent perfect crystals and bent mosaic crystals are similar in this respect - it is only the degree of blurring that is different. For bent perfect crystals the blurring is defined by the ratio between the crystal thickness and the horizontal radius of curvature. Typically this is much smaller than the blurring due to the mosaic spread. The crystal thickness is also much smaller than the crystal lateral extent. Relations (5) define thus the inclination of the acceptance window in the  $(k\gamma, \Delta k)$  plane of the phase space.

In contrast with the diffraction by mosaic crystals, the diffraction by perfect crystals is basically a deterministic process. This is implicit in the matrix formulation of neutron optics codes [2,4,5]. To describe analytically the blurring due to the crystal thickness an explicit formulation is also needed. The change of neutron state on diffraction is described by a  $3 \times 3$

reflection matrix relating the horizontal vectors  $\boldsymbol{\eta}_l$  and  $\boldsymbol{\eta}_0$ . The coordinates of the point in the crystal where diffraction takes place are eliminated in the process. However, they are accounted for in the boundaries of the phase space acceptance window.

In the first order (linear, or paraxial) approximation the relations describing the local diffraction conditions inside a deformed moving crystal, obtained by expanding in projections the Bragg relation in vector form, can be written as:

$$\begin{aligned} (\gamma_1 - \gamma_0) \cot \theta + \left( \frac{\Delta k_1}{k} + \frac{\Delta k_0}{k} \right) &= 2 \frac{\Delta \tau_1}{\tau} \\ (\gamma_1 + \gamma_0) - \left( \frac{\Delta k_1}{k} - \frac{\Delta k_0}{k} \right) \cot \theta &= 2 \frac{\Delta \tau_2}{\tau} \\ \frac{\Delta k_1}{k} - \frac{\Delta k_0}{k} &= 2 \sin \theta \cos \chi \frac{v_1}{v_n} \end{aligned} \quad (6)$$

The diffraction geometry in the reciprocal space is presented in Fig. 1. To calculate the neutron trajectories before and after reflection it is necessary to know the spatial variation of  $\Delta \tau_1$ ,  $\Delta \tau_2$  and  $v_1$  (local lattice velocity component along  $\boldsymbol{\tau}_0$ ) inside the crystal. In the general case one has to the first order the following matrix relation:

$$\begin{bmatrix} \frac{\Delta \tau_1}{\tau} \\ \frac{\Delta \tau_2}{\tau} \\ \sin \theta \cos \chi \frac{v_1}{v_n} \end{bmatrix} = \begin{bmatrix} a_{11} & a_{12} \\ a_{21} & a_{22} \\ a_{31} & a_{32} \end{bmatrix} \times \begin{bmatrix} l_M \\ g_M \end{bmatrix} \quad (7)$$

The orthogonal coordinates inside the crystal can be expressed through the coordinates of the point where diffraction occurs, taken across the incident and diffracted beam:

$$\begin{bmatrix} l_M \\ g_M \end{bmatrix} = \begin{bmatrix} c_- & -c_+ \\ -s_- & -s_+ \end{bmatrix} \times \begin{bmatrix} y_0 \\ y_1 \end{bmatrix} \quad (8)$$

The diffraction geometry is presented in Fig. 2. The trigonometric functions  $s_+$ ,  $s_-$ ,  $c_+$ ,  $c_-$  are defined in the notation summary. To simplify the expressions a new matrix is introduced which directly connects the vector defined in the left side of (7) with the coordinates  $y_0$  and  $y_1$ :

$$\begin{bmatrix} b_{11} & b_{12} \\ b_{21} & b_{22} \\ b_{31} & b_{32} \end{bmatrix} = \begin{bmatrix} a_{11} & a_{12} \\ a_{21} & a_{22} \\ a_{31} & a_{32} \end{bmatrix} \times \begin{bmatrix} c_- & -c_+ \\ -s_- & -s_+ \end{bmatrix} \quad (9)$$

From relations (6) and the matrix defined in (9) the reflection matrix results:

$$\begin{bmatrix} y_1 \\ \gamma_1 \\ \frac{\Delta k_1}{k} \end{bmatrix} = \begin{bmatrix} C_{11} & C_{12} & C_{13} \\ C_{21} & C_{22} & C_{23} \\ C_{31} & C_{32} & C_{33} \end{bmatrix} \times \begin{bmatrix} y_0 \\ \gamma_0 \\ \frac{\Delta k_0}{k} \end{bmatrix} \quad (10)$$

where:

$$\begin{aligned} C_{11} &= (b_{11} - b_{21} \cot \theta - b_{31} / \sin^2 \theta) / D \\ C_{12} &= \cot \theta / D \\ C_{13} &= -1 / D \\ C_{21} &= 2[b_{11}b_{22} - b_{12}b_{21} + b_{21}b_{32} - b_{22}b_{31} + (b_{11}b_{32} - b_{12}b_{31}) \cot \theta] / D \\ C_{22} &= [b_{12} + b_{22} \cot \theta - b_{32}(1 - \cot^2 \theta)] / D \\ C_{23} &= -2(b_{22} + b_{32} \cot \theta) / D \\ C_{31} &= 2[b_{11}b_{32} - b_{12}b_{31} - (b_{21}b_{32} - b_{22}b_{31}) \cot \theta] / D \\ C_{32} &= 2b_{32} / D \\ C_{33} &= [-b_{12} + b_{22} \cot \theta - b_{32}(1 - \cot^2 \theta)] / D \\ D &= -b_{12} + b_{22} \cot \theta + b_{32} / \sin^2 \theta \end{aligned} \quad (10')$$

The constraint matrix defining the phase space acceptance diagram is derived similarly.

From relations (6) it results:

$$-\gamma_0 \cot \theta + \frac{\Delta k_0}{k} = \frac{\Delta \tau_1}{\tau} - \frac{\Delta \tau_2}{\tau} \cot \theta - \frac{\cos \chi}{\sin \theta} \frac{v_1}{v_n} \quad (11)$$

while by definition one has:

$$y_0 = l_M \sin(\theta + \chi) - g_M \cos(\theta + \chi) \quad (12)$$

By using (11) and (12) one obtains expressions for the elements of the constraint matrix. This is the matrix relating the true crystal coordinates  $l_M$  and  $g_M$  with the variables of the neutron path before reflection  $y_0$ ,  $\gamma_0$ ,  $\Delta k_0/k$ :

$$\begin{bmatrix} l_M \\ g_M \end{bmatrix} = \begin{bmatrix} \frac{\Gamma_{02}}{\Gamma_{00}} & \frac{-\cot \theta \cos(\theta + \chi)}{\Gamma_{00}} & \frac{\cos(\theta + \chi)}{\Gamma_{00}} \\ -\frac{\Gamma_{01}}{\Gamma_{00}} & \frac{-\cot \theta \sin(\theta + \chi)}{\Gamma_{00}} & \frac{\sin(\theta + \chi)}{\Gamma_{00}} \end{bmatrix} \times \begin{bmatrix} y_0 \\ \gamma_0 \\ \frac{\Delta k_0}{k} \end{bmatrix} \quad (13)$$

where:

$$\begin{aligned}
\Gamma_{01} &= a_{11} - a_{21} \cot \theta - a_{31} / \sin^2 \theta \\
\Gamma_{02} &= a_{12} - a_{22} \cot \theta - a_{32} / \sin^2 \theta \\
\Gamma_{00} &= \Gamma_{01} \cos(\theta + \chi) + \Gamma_{02} \sin(\theta + \chi)
\end{aligned} \tag{13'}$$

In a similar way the constraint relations after diffraction are derived:

$$\begin{bmatrix} l_M \\ g_M \end{bmatrix} = \begin{bmatrix} -\frac{\Gamma_{12} - \cot \theta \cos(\theta - \chi) \cos(\theta - \chi)}{\Gamma_{10}} & \frac{\Gamma_{10}}{\Gamma_{10}} & \frac{\Gamma_{10}}{\Gamma_{10}} \\ \frac{\Gamma_{11}}{\Gamma_{10}} & \frac{\cot \theta \sin(\theta - \chi)}{\Gamma_{10}} & \frac{\sin(\theta - \chi)}{\Gamma_{10}} \end{bmatrix} \times \begin{bmatrix} y_1 \\ \gamma_1 \\ \frac{\Delta k_1}{k} \end{bmatrix} \tag{14}$$

where:

$$\begin{aligned}
\Gamma_{11} &= a_{11} + a_{21} \cot \theta + a_{31} / \sin^2 \theta \\
\Gamma_{12} &= a_{12} + a_{22} \cot \theta + a_{32} / \sin^2 \theta \\
\Gamma_{10} &= -\Gamma_{11} \cos(\theta - \chi) + \Gamma_{12} \sin(\theta - \chi)
\end{aligned} \tag{14'}$$

By assuming  $g_M=0$  in relations (13) and (14), the general correlation for the thin crystal case, an extension of relation (5), is obtained as follows:

$$\begin{aligned}
\frac{\Delta k_0}{k} &= -\cot \theta \frac{y_0}{2f_0^*} - \cot \theta \left( \frac{L_0}{2f_0^*} - 1 \right) \gamma_0 \\
\frac{\Delta k_1}{k} &= -\cot \theta \frac{y_1}{2f_1^*} + \cot \theta \left( \frac{L_1}{2f_1^*} - 1 \right) \gamma_1
\end{aligned} \tag{15}$$

where:

$$\begin{aligned}
\frac{1}{2f_0^*} &= \frac{-a_{11} \tan \theta + a_{21} + \frac{2a_{31}}{\sin 2\theta}}{\sin(\theta + \chi)} \\
\frac{1}{2f_1^*} &= \frac{a_{11} \tan \theta + a_{21} + \frac{2a_{31}}{\sin 2\theta}}{\sin(\theta - \chi)}
\end{aligned} \tag{15'}$$

The distances  $f_0^*, f_1^*$  differ from the real focal lengths  $f_0, f_1$ . To calculate these focal lengths one considers the transport to the crystal of neutrons from a plane located at a distance  $L_0$  before the crystal and the subsequent transport from the crystal to a plane located at a distance  $L_1$  after the crystal. Relation (10) becomes:

$$\begin{bmatrix} y_1 \\ \gamma_1 \\ \frac{\Delta k_1}{k} \end{bmatrix} = \begin{bmatrix} 1 & L_1 & 0 \\ 0 & 1 & 0 \\ 0 & 0 & 1 \end{bmatrix} \times \begin{bmatrix} C_{11} & C_{12} & C_{13} \\ C_{21} & C_{22} & C_{23} \\ C_{31} & C_{32} & C_{33} \end{bmatrix} \times \begin{bmatrix} 1 & L_0 & 0 \\ 0 & 1 & 0 \\ 0 & 0 & 1 \end{bmatrix} \times \begin{bmatrix} y_0 \\ \gamma_0 \\ \frac{\Delta k_0}{k} \end{bmatrix} \quad (16)$$

By inserting into this relation the first constraint of (15) and by canceling the coefficient of  $\gamma_0$  in the expression of  $y_1$ , the lens relation for thin bent crystals is obtained with general equations for the focal lengths:

$$\frac{\sin(\theta + \chi)}{2f_0} = \frac{\sin(\theta - \chi)}{2f_1} = a_{21} + a_{31} \cot \theta \quad (17)$$

The lens formula (4) with the focal lengths defined by (17) ensures that while diffraction occurs on the neutral surface of the crystal or on a surface parallel to it, all neutrons emitted from a point are collected to a point.

### 2.3. Elastically bent crystal

The variation of the reciprocal lattice vector in an elastically deformed crystal was examined previously [3]. The following reflection matrix describes the Bragg reflection in this case [16]:

$$\begin{bmatrix} y_1 \\ \gamma_1 \\ \frac{\Delta k_1}{k} \end{bmatrix} = \begin{bmatrix} \alpha_0 & -2f & 2f \tan \theta \\ \frac{1 - \alpha_0 \alpha_1}{2f} & \alpha_1 & -(1 + \alpha_1) \tan \theta \\ 0 & 0 & 1 \end{bmatrix} \times \begin{bmatrix} y_0 \\ \gamma_0 \\ \frac{\Delta k_0}{k} \end{bmatrix}, \quad (18)$$

where

$$f = \frac{R_e \sin 2\theta \operatorname{sgn}(\theta + \chi)}{2G}; G = \cos(\theta + \chi) + (A \tan \theta + B) \sin(\theta + \chi); \quad (18')$$

$$\alpha_0 = \frac{f - f_1}{f_0}; \alpha_1 = \frac{f - f_0}{f_1}.$$

Physically  $G/R_e$  represents the change in Bragg angle per unit incident neutron pathlength in the crystal [3]. A and B can be represented as function of a single material size ( $\kappa$ ) as follow:

$$\begin{aligned} A &= 1 - (1 + \kappa) \cos^2 \chi \\ B &= (1 + \kappa) \sin \chi \cos \chi \end{aligned} \quad (18'')$$



This constant  $\kappa$  accounts for the lattice elastic deformation normal to the crystal plate. It depends of the crystal shape and the crystallographic orientation of the plate [18]. If the curvature comes from an in-depth gradient of d-spacing (thermal or compositional) then in relations (18') one should put  $A = I$  and  $B = 0$ .

The reflection matrix in (18) is unitary - its determinant equals unity. The phase space volume is thus preserved upon the transformation (18), as required by the Liouville theorem (which actually says that the neutron density in the phase space cannot increase). Relation (18) is valid regardless of crystal dimensions. The crystal dimensions only define the phase space acceptance window through the relation [16]:

$$\left[ \begin{array}{c} -\frac{g_M^{\max}}{2} \\ -\frac{l_M^{\max}}{2} \end{array} \right] \leq \left[ \begin{array}{cc} -s_+ \frac{f}{f_0} & 2s_+ f \\ -c_+ \frac{f}{f_0} + \frac{R_e \operatorname{sgn}(\theta + \chi)}{2f_0} & 2c_+ f \end{array} \right] \times \left[ \begin{array}{c} y_0 \\ \gamma_0 \\ \frac{\Delta k_0}{k} \end{array} \right] \leq \left[ \begin{array}{c} \frac{g_M^{\max}}{2} \\ \frac{l_M^{\max}}{2} \end{array} \right], \quad (19)$$

where  $g_M^{\max}, l_M^{\max}$  are the crystal thickness and lateral extension respectively, and  $s_+, c_+$  are trigonometric functions (see notation summary). Similar relations hold for the diffracted beam. Relations (18,19) refer to neutron states at points within the crystal. To find the relations at points before and after reflection, transport matrices as in relation (16) multiply reflection matrices, with the difference that these are now  $3 \times 3$  matrices.

#### 2.4. Bent packets of wafers

Each bent wafer of a packet reflects neutrons like a bulk crystal and has its individual acceptance window in the phase space. The overall acceptance window has a complex shape and generally is sparsely filled. The effective peak reflectivity is an average over the whole acceptance window. When individual acceptance windows superimpose, corrections must be introduced in the peak reflectivity to account for possible losses due to multiple reflections [16].

To describe packets of wafers a simple model will be used: that of a bulk bent crystal of a thickness corresponding to the total thickness of the packet but with no elastic stresses (*ideal bending*,  $A=0, B=0$ ). The results will be only approximate, the degree of approximation being given by the thickness of a single wafer. The reflection matrix for this important case is [16]:

$$\begin{bmatrix} y_1 \\ \gamma_1 \\ \frac{\Delta k_1}{k} \end{bmatrix} = \begin{bmatrix} \frac{L_1^*}{L_0^*} & -2L_1^* & 2L_1^* \tan \theta \\ 0 & 1 & -2 \tan \theta \\ 0 & 0 & 1 \end{bmatrix} \times \begin{bmatrix} y_0 \\ \gamma_0 \\ \frac{\Delta k_0}{k} \end{bmatrix}, \quad (20)$$

where

$$L_0^* = \frac{R_e \sin 2\theta \operatorname{sgn}(\theta + \chi)}{2 \cos(\theta - \chi)}; L_1^* = \frac{R_e \sin 2\theta \operatorname{sgn}(\theta + \chi)}{2 \cos(\theta + \chi)}. \quad (20')$$

The determinant of the reflection matrix is  $\cos(\theta - \chi)/\cos(\theta + \chi)$ . It differs from unity if the reflection is asymmetric. The overall volume in the phase space diagram may thus be different before and after reflection. This is an apparent violation of the Liouville theorem, introduced by the approximation used in modeling. In reality no violation occurs, as each individual wafer does obey the Liouville theorem. To correct for this, a factor must be introduced in the average peak reflectivity, which depends on whether the phase space volume considered on averaging is before or after reflection [16]. This only matters for intensity calculations. We will focus here on optical properties and will assume that the conservation of phase space density is ensured through peak reflectivities.

In the multi-wafer case relations (19) become [16]:

$$\begin{bmatrix} -\frac{g_M^{\max}}{2} \\ -\frac{l_M^{\max}}{2} \end{bmatrix} \leq \begin{bmatrix} \frac{1}{\cos(\theta + \chi)} & \frac{2f_0}{\cos(\theta + \chi)} & -\frac{2f_0}{\cos(\theta + \chi)} \tan \theta \\ 0 & \frac{2f_0}{\sin(\theta + \chi)} & -\frac{2f_0}{\sin(\theta + \chi)} \tan \theta \end{bmatrix} \times \begin{bmatrix} y_0 \\ \gamma_0 \\ \frac{\Delta k_0}{k} \end{bmatrix} \leq \begin{bmatrix} \frac{g_M^{\max}}{2} \\ \frac{l_M^{\max}}{2} \end{bmatrix} \quad (21)$$

The wafer packet was considered parallel, with the wafers fully in contact on adjacent surfaces. If adjacent wafers are not in contact and relative tilts are introduced then  $B \neq 0$  and formulae (20) and (21) will change.

### 3. Imaging conditions

Consider the transfer of a neutron from a point at a distance  $L_0$  before the crystal to a point at a distance  $L_1$  after the crystal. The general expression (16) can be rearranged as follow:

$$\begin{bmatrix} y_1 \\ \gamma_1 \\ \frac{\Delta k_1}{k} \end{bmatrix} = \begin{bmatrix} C_{11} + L_1 C_{21} & C_{12} + L_0 C_{11} + L_1 C_{22} + L_0 L_1 C_{21} & C_{13} + L_1 C_{23} \\ C_{21} & C_{22} & C_{23} \\ C_{31} & C_{32} & C_{33} \end{bmatrix} \times \begin{bmatrix} y_0 \\ \gamma_0 \\ \frac{\Delta k_0}{k} \end{bmatrix} \quad (16')$$

The structure of this matrix gives an interesting result: neutrons emerging from a point at  $L_0$  are imaged into a point at  $L_1$  when the following correlation between  $\gamma_0$  and  $\Delta k_0/k$  exists:

$$(C_{12} + L_0 C_{11} + L_1 C_{22} + L_0 L_1 C_{21})\gamma_0 + (C_{13} + L_1 C_{23})\frac{\Delta k_0}{k} = 0 \quad (22)$$

In the general case relation (22) says that a point of the object space may be imaged into different points of a line. Every point of the line in the diffraction plane will correspond to a distinct path in the wavevector plane ( $k\gamma_0$ ,  $\Delta k_0$ ). The line image will furnish a spectral analysis of the object, analogous to what a prism does in conventional optics. Only a small part of the crystal will contribute to the formation of each image point. Different zones of the crystal will give different points of the image. We call this *dispersive imaging* [18]. Illustrative cases are discussed below.

### 3.1. Dispersive chromatic imaging

*Dispersive chromatic imaging* occurs when all neutrons coming from a point and having the same wavevector are focused to the same point regardless of their direction [15]. It occurs when the coefficient of  $\gamma_0$  in (22) vanishes:

$$C_{12} + L_0 C_{11} + L_1 C_{22} + L_0 L_1 C_{21} = 0 \quad (23)$$

For multi-wafer packets a simple expression is obtained [15]:

$$\frac{L_0}{L_0^*} + \frac{L_1}{L_1^*} = 2. \quad (24)$$

For elastically bent bulk crystals the exact condition is:

$$\left(\frac{2f}{L_0} - \alpha_0\right) \times \left(\frac{2f}{L_1} - \alpha_1\right) = 1, \quad (25)$$

with  $f$ ,  $\alpha_0$  and  $\alpha_1$  given by relation (18').

The condition of dispersive chromatic imaging should not be confused with the monochromatic focusing condition for thin bent crystals  $2f_0/L_0=1$ . At monochromatic focusing all neutrons reflected from along the crystal have the same energy. In the case under

consideration the crystal is an analyzer that images neutrons with different energies into different points. The energy spectrum of the incoming beam is converted by Bragg reflection into a spatial distribution at the distance  $L_I$ . If the beam is strictly monochromatic the image of a point is again a point. Conditions (24) or (25) specify arrangements with good energy resolution using a point neutron source, a curved crystal analyzer, and a PSD.

### 3.2. Dispersive angular imaging

*Dispersive angular imaging* occurs when all neutrons coming from a point along a certain direction are focused to a point regardless of the wavevector. The angular distribution of the incoming beam is converted into a spatial distribution. The corresponding condition is obtained by canceling the coefficient of  $\Delta k_0/k$  in the expression of  $y_I$  in relation (22):

$$C_{13} + L_1 C_{23} = 0 \quad (26)$$

This relation involves only the distance from crystal to image  $L_I$ . A general condition for  $L_I$  can be derived in terms of the primary coefficients  $a_{ij}$  defined in (7):

$$\frac{1}{2L_1} = (a_{21} + a_{31} \cot \theta) c_+ + (a_{22} + a_{32} \cot \theta) s_+ \quad (27)$$

In the case of an elastically bent bulk plate this simplifies to:

$$L_1 = \frac{L_1^*}{1 + B \tan(\theta + \chi)} \quad (28)$$

For multi-wafer packets relation (28) reduces to  $L_1 = L_1^*$ , see relation (20').

### 3.3. Non-dispersive imaging - Bragg mirrors

The previous imaging conditions cancel the contributions of the angular spread or the wavevector spread (or a linear combination thereof) to the image spread of a point. The object point is then imaged into a line along which some physical quantity varies (wavevector, wavevector transfer, energy transfer, etc). The distribution of that physical quantity is converted into a spatial distribution. If the task is to obtain a real image of the object then the image of a point must not be a line but a point. Then, the arrangement must be non-dispersive, that is the spatial dispersion of the beam must be canceled. The contributions to the blurring from both the angular spread and the wavevector spread must vanish. Then the crystal becomes a *Bragg mirror* (BM) - an imaging device with no chromatic aberrations (Fig. 3).

For the crystal to be a Bragg mirror the coefficients of both the  $\gamma_0$  and  $\Delta k_0/k$  terms of  $y_l$  in relation (22) must vanish simultaneously:

$$\begin{aligned} C_{12} + L_0 C_{11} + L_1 C_{22} + L_0 L_1 C_{21} &= 0, \\ C_{13} + L_1 C_{23} &= 0 \end{aligned} \quad (29)$$

or, equivalently:

$$L_0 = -\frac{\begin{vmatrix} C_{12} & C_{13} \\ C_{22} & C_{23} \end{vmatrix}}{\begin{vmatrix} C_{11} & C_{13} \\ C_{21} & C_{23} \end{vmatrix}}; L_1 = -\frac{C_{13}}{C_{23}}. \quad (29')$$

By expressing the coefficients of the reflection matrix  $C_{ij}$  through the primary coefficients  $a_{ij}$  of the reciprocal lattice vector simple closed relations are obtained:

$$\begin{aligned} \frac{1}{2L_0} &= (a_{21} + a_{31} \cot \theta)c_- - (a_{22} + a_{32} \cot \theta)s_- \\ \frac{1}{2L_1} &= (a_{21} + a_{31} \cot \theta)c_+ + (a_{22} + a_{32} \cot \theta)s_+ \end{aligned} \quad (30)$$

with  $s_+$ ,  $s_-$ ,  $c_+$ ,  $c_-$  trigonometric functions given in notation summary and with special cases as follow:

- multi-wafer packet:

$$L_0 = L_0^*, L_1 = L_1^*; \quad (30a)$$

- elastic bending of a bulk plate:

$$L_0 = \frac{L_0^*}{1 - B \tan(\theta - \chi)}, L_1 = \frac{L_1^*}{1 + B \tan(\theta + \chi)}; \quad (30b)$$

### 3.4. Stigmatic Bragg mirrors

A mirror is *astigmatic* if the image positions in the equatorial and sagittal planes are different. The astigmatism of the BM is canceled (*stigmatic imaging*) when the lens focusing relation in the vertical plane is also fulfilled:

$$\frac{f_a}{L_0} + \frac{f_a}{L_1} = 1, f_a = \frac{R_a}{2 \cos \chi |\sin \theta|}. \quad (31)$$

By inserting (30) into (31) a simple general condition of *stigmatic imaging* is obtained:

$$\frac{\sin^2 \theta}{R_a} = a_{21} + a_{32} + a_{22} \tan \theta + a_{31} \cot \theta \quad (32)$$

with special cases as follow:

- multi-wafer packet with ideal bending:

$$R_a = R_e \operatorname{sgn}(\theta + \chi) \sin^2 \theta \quad (32a)$$

- elastic bending of a bulk plate:

$$R_a = \frac{R_e \operatorname{sgn}(\theta + \chi) \sin^2 \theta}{1 + B \tan \theta} \quad (32b)$$

## 4. Bragg Mirror imaging resources

### 4.1. Working zones

The magnification of the BM is given by the distance ratio:

$$M = \frac{L_1}{L_0} = \frac{(a_{21} + a_{31} \cot \theta)c_- - (a_{22} + a_{32} \cot \theta)s_-}{(a_{21} + a_{31} \cot \theta)c_+ + (a_{22} + a_{32} \cot \theta)s_+}. \quad (33)$$

For multi-wafer packets the magnification is simply:

$$M = \frac{\cos(\theta - \chi)}{\cos(\theta + \chi)} \quad (33')$$

Only when  $M > 0$  is the image real and only then can a BM provide an image on a PSD. The BM working zones for ideal bending are sketched in Fig. 4 as a function of the take-off angle  $2\theta$  and  $\alpha = \theta + \chi$  (BM inclination angle relative to the incoming beam). Reflection arrangements are permitted at any take-off angle.

A Bragg mirror can be used to focus a divergent beam from a small source or a well-collimated beam from an extended source. In the first case the image size is determined by the magnification:  $\Delta y_1 = M \Delta y_0$ . In the second case  $L_1 = f_1$  with  $f_1$  defined by the general relation (17) and the image size is determined by the angular divergence of the collimator  $\Delta y_1 = L_1 \Delta \gamma_0$ . In both cases the real image is sharp even if the crystal is thick. For radiography applications a virtual image may be of interest, in which case the same conditions are valid but suitable arrangements with  $L_1 \leq 0$  should be considered.

#### 4.2. Image resolution

The image spatial resolution is determined by the optical quality of the BM and by the spatial resolution of the PSD, because the image blurring due to the intrinsic diffraction range in a perfect crystal is usually negligible (less than  $5 \mu\text{m}$  at  $1\text{m}$ ). The ultimate resolution in imaging is set by the thickness of the individual wafers in the analyzer packet. With inexpensive standard silicon wafers a spatial resolution around  $1 \text{ mm}$  is easily reached (see demonstration experiment described below). This resolution is already better than that planned to be achieved with SMARTS\* instrument at the Los Alamos Neutron Science Center (LANSCE) and is comparable with the resolution achieved at the ORNL reactor HFIR where residual stress mapping is obtained by sequential stepping.

For multi-wafer option the main aberration term comes from the elastic deformation of the wafer. By curving the wafer a tangential stress gradient is generated inside the crystal. This gradient not only changes the d-spacing, but also rotates the crystalline planes if they are not parallel to the crystal surface. Qualitatively, the wafer deformation aberration term will be proportional to  $\sin\chi$  and the wafer thickness. Consequently this term vanishes when  $\chi = 0$  and otherwise can be minimized by using thinner wafers available commercially at thickness down to  $10 \text{ microns}$ , although the mechanics of their assembly would be complicated. High-order aberrations may also come into play. Conditions can be found, though, to minimize those aberrations and to even cancel them. A careful theoretical and experimental investigation is needed to quantify the ultimate resolution in imaging. The practical limit is expected to be around  $100 \text{ microns}$ . A very high accuracy of bending will be needed to achieve that limit.

#### 4.3. Imaging high order aberrations

The geometrical theory of aberrations for BM is complicated by the fact that there is only a plane of symmetry, instead of an axis as in the case of an optical lens, but aberration types are similar. Considering the image of the central object point, the equatorial ( $\Delta y_1$ ) and axial ( $\Delta z_1$ ) deviations can be expressed as a series expansion of the ray coordinates on the mirror ( $l_M, z_M, g_M$ ):

$$\frac{\Delta y_1}{L_1} = A_{ijk} l_M^i z_M^j g_M^k \quad \text{and} \quad \frac{\Delta z_1}{L_1} = B_{ijk} l_M^i z_M^j g_M^k \quad (34)$$

---

\* SMARTS will be the world's best special mapping instrument based on design objectives.

In practice only a few terms are significant:

$$\begin{aligned}\frac{\Delta y_1}{L_1} &= A_{100}l_M + A_{001}g_M + A_{200}l_M^2 + A_{020}z_M^2 + A_{300}l_M^3 + A_{120}l_M z_M^2 \\ \frac{\Delta z_1}{L_1} &= B_{010}z_M + B_{110}l_M z_M + B_{210}l_M^2 z_M + B_{030}z_M^3\end{aligned}\quad (34')$$

The aberration type was designated by analogy with the light optics:  $A_{100}$  corresponds to *defocusing*,  $B_{001}$  to *astigmatism*,  $A_{002}$  to *coma*,  $A_{020}$  and  $B_{110}$  to *astigmatic coma*,  $A_{300}$ ,  $A_{120}$ ,  $B_{210}$  and  $B_{030}$  to *generalized spherical aberrations*. The *thickness aberration* is described in the first approximation by  $A_{001}$ . This *thickness aberration* can be assimilated to the optical chromatic aberration and is in fact canceled when the non-dispersive imaging condition is fulfilled.

Using the following notation the first and second order aberration coefficients have simple expressions:

$$\begin{aligned}A_{100} &= C_{e1} + C_{e2} \\ A_{001} &= D_2 - D_1 \\ A_{200} &= \frac{3}{2}(D_2 C_{e2} - D_1 C_{e1}) \\ A_{002} &= \frac{1}{2}(D_2 C_{a2} - D_1 C_{a1}) \\ B_{010} &= C_{a1} + C_{a2} \\ B_{110} &= 2A_{002}\end{aligned}\quad ; \quad \begin{aligned}C_{e1} &= \frac{\sin(\theta + \chi)}{L_0} - \frac{1}{R_e} \\ C_{e2} &= \frac{\sin(\theta - \chi)}{L_1} - \frac{1}{R_e} \\ C_{a1} &= \frac{1}{L_0} - \frac{\sin(\theta + \chi)}{R_a} \\ C_{a2} &= \frac{1}{L_1} - \frac{\sin(\theta - \chi)}{R_a} \\ D_1 &= \frac{\cos(\theta + \chi)}{L_0} \\ D_2 &= \frac{\cos(\theta - \chi)}{L_1}\end{aligned}\quad . \quad (35)$$

The third order aberration coefficients have complex analytical expressions depending on the real mirror shape (bicycle tire toroidal, barrel toroidal, ellipsoidal, etc.).

By canceling the first order aberration coefficients the relations (30a) and (32a) are obtained. The first two conditions (30a) are required for aberration-free one-dimensional imaging in the equatorial plane and the last condition (32a) is required to reduce the astigmatism. Different radii of curvature in the equatorial and axial planes are thus necessary for two-dimensional imaging with BM.

By introducing these relations in the expressions of second order aberration coefficients, simple formula are obtained:



$$A_{200} = -\frac{3}{2} \times \frac{\sin 2\chi}{L_0 L_1} \quad \text{and} \quad A_{020} = \frac{\sin \chi \cos 2\theta}{\sin \theta} \times \frac{1}{L_0 L_1} \quad (36)$$

Thus the second order coma and astigmatic coma are zero when  $\chi = 0$ .

Then for thin wafers the ultimate spatial resolution is defined by the influence of higher order aberrations as follow:

- If the crystal cutting angle  $\chi$  is different from 0, the second order coma and astigmatic coma are the main aberration sources. Matching these contributions with the first order thickness and astigmatism contributions can minimize the loss of spatial resolution.
- For  $\chi = 0$  these aberrations vanish and the third order generalized spherical aberrations are relevant. These aberrations are shape sensitive and can be minimized by choosing the crystal profile.

The aberrations introduced by object (sample) extension (field curvature and distortion) are sensitive to the PSD configuration and can be partially corrected by digital image processing.

## 5. Testing the Bragg Mirror concept

To demonstrate imaging with BM an experiment was done at the High Flux Isotope Reactor (HFIR) of the Oak Ridge National Laboratory (ORNL). A thick multi-wafer assembly designed and fabricated at the University of Missouri Research Reactor (MURR) [15,16] was used. The assembly consisted of 14 commercial wafers, each 20 cm wide and 0.7 mm thick, originating from the same [100] ingot. The horizontal radius of curvature  $R_e$  was set by a 4-point elastic bending device and was adjustable with a fine screw. The vertical curvature was approximated by fine segmentation (5 mm). The vertical radius  $R_a$  was set by the profile of the bending posts (barrel shaped on the front, concave on the back) and was fixed at 1.38 m. Because the vertical radius was fixed and the vertical curvature was obtained by segmentation, the astigmatism was not canceled in this experiment.

To simulate the object a cadmium foil with three slits, each 2 mm wide, was put in the beam produced by a flat mosaic Ge monochromator ( $\lambda=1.26 \text{ \AA}$ ). The image formation was observed with a neutron camera. After adjustment of angle, distances and horizontal radius to fulfil the condition (30a) of non-dispersive imaging, the image was registered on Polaroid film. The results are presented in Fig. 5. The neutron beam after the slits is shown in Fig. 5a. The

neutron beam before the monochromator is shown in Fig. 5b. The multi-wafer monochromator was placed at 1 m after the object slits.

Two different configurations were tested: reflection Si (400) with unit magnification and reflection Si (511) with 1.5 magnification in the diffraction plane. The neutron beams at the two imaging positions are shown in Figs. 5c and 5d. The image sharpness demonstrates a spatial resolution in the horizontal plane corresponding to the thickness of one wafer (0.7 mm), at a total thickness of the packet of 1 cm.

The image clarity is strongly dependent of BM curvature radius and the distance to the film position. The Figure 6 illustrates the neutron beam profile variation with the distance between BM and film. The decrease of intensity in the middle of the image results from a gap between the two central strips of the multi-wafer assembly. The BM tilt is responsible for the overall inclination of the image relative to the slit position.

The image clarity is also affected by the neutron converter thickness. For this reason it was impossible to observe a clear image formation directly on the screen of a neutron camera. Only a thin converter before the Polaroid film could provide a clear image.

Another test measurement was completed at the HFIR residual stress facility in which the thick multi-wafer assembly was located to reflect neutrons scattered by a sample and a PSD was used to detect the neutrons. To evaluate the spatial resolution the cadmium foil with three slits used in the previous experiment was placed in front of PSD. The spatial pattern registered by PSD in a collimated beam ( $<1^\circ$  angular divergence) is presented in fig. 7. The PSD contribution can be well described by a Gaussian profile with 2.75(7) mm FWHM (see fig.7). An additional increase of FWHM up to 3.2 mm was observed at a larger angular divergence of the incoming neutron beam.

The experimental set-up is sketched in fig. 8. The existing silicon monochromator provided a monochromatic beam with  $\lambda=1.67 \text{ \AA}$ . Two different samples were tested for imaging in scattering: a vanadium plate 2 mm thick and an iron pin (diameter of  $\sim 2 \text{ mm}$ ). The multi-wafer assembly with Si(400) reflection intercepts the scattered neutron beam and provides the image of the sample on PSD (fig. 8). For the iron pin sample the multi-wafer assembly was placed at  $81.9^\circ$  scattering angle corresponding to the diffraction line (211). For the vanadium plate the neutron scattering is elastic incoherent and isotropic, consequently the scattering angle was chosen from alignment reasons at  $86.9^\circ$ . The plate was oriented along the scattered beam in order to minimize

the spatial extension of the scattered neutron beam at sample position. The distances from sample to multi-wafer and from multi-wafer to PSD were almost equal (1.09 m).

The multi-wafer assembly curvature was varied in order to obtain the densest image. The FWHM of the spatial pattern registered by PSD is presented in Fig. 9. The optimal curvature is slightly different from the theoretical value but the difference is not really significant in such test experiments. In contrast, the minimal FWHM-s of images (2-3 mm) are encouraging enough. The image is naturally wider for the vanadium plate as the whole analyzer is contributing to the image formation and all geometrical contributions to the image smearing are significantly amplified by comparison with the diffraction case when the scattered beam is spatially limited.

## 6. Bragg mirrors at pulsed sources

A BM can also be used for neutron imaging at pulsed neutron sources. Then the incident neutron energy is determined by time-of-flight. Using a two-dimensional (2D) position sensitive detector (PSD) and time-of-flight (TOF) analysis the BM imaging system (BMIS) will make it possible to collect both real space mappings and scattering space data simultaneously, enabling totally new research opportunities. In the time-of-flight method each pixel of the PSD contains a segment of the diffraction pattern, useful for strain, texture or phase fraction mapping, or an inelastic scattered spectrum. The image may refer to any scattering law, for either elastic or inelastic scattering.

### 6.1. Phase space acceptance diagram

The acceptance window in phase space provides a complete characterization of a BM. This is similar to the acceptance diagrams defined in two dimensions (spatial and angular), but is five dimensional ( $x, y, \gamma, \delta, \Delta k/k$ ). If one restricts the discussion to a point source and accepts the approximation that the vertical angular deviation does not influence the acceptance in the horizontal plane, then the relevant phase space acceptance diagram for a BM can be reduced to two dimensions ( $\gamma, \Delta k/k$ ).

For inelastic scattering the range of accepted wavelengths will define the instrument resolution. For diffraction (or incoherent elastic scattering) the shape of the phase space acceptance diagram does not have a decisive influence on the instrument resolution, but drastically reduces the range of accessible wavevector transfers. BMs have to be adjusted to transmit the phase space field corresponding to the wavevector transfer of interest. It is important

to note that for a fixed radius of BM the inclination of the needle-shaped acceptance diagram is determined by the cutting angle  $\chi$  only, the length is determined by the mirror lateral extent and the width is determined by the mirror thickness.

- If  $\chi = 0$  the relative wavelength window  $(\Delta\lambda/\lambda)_{max}$  is not influenced by the angular acceptance. Therefore a narrow energy resolution (down to 1%) can be obtained for inelastic scattering in this case. A large angular acceptance (about  $\sim 10^\circ$  in both the equatorial and axial plane), determined by the BM dimensions, ensures a high rate of data collection.
- If  $\chi \neq 0$  the wavevector value and direction are correlated and large wavelength windows of up to  $(\Delta\lambda/\lambda)_{max} \approx 10\%$  can be obtained. Such asymmetric configurations are appropriate for elastic scattering when the wavelength value is determined by time-of-flight. In this case the angular acceptance at fixed wavelength is determined by the BM thickness (about  $1^\circ$  per cm).

The multiwafer BM phase space acceptance diagram is in fact a superposition of the individual acceptance diagrams for each wafer. Because of elastic lattice deformation, gaps or superpositions can appear between these individual diagrams and reflectivity oscillations may result. There exists a certain optimal combination of  $\theta$  and  $\chi$  where the individual diagrams stay adjacent and the oscillations disappear namely when  $|G|$  [defined in (18')] becomes equal to  $|\cos(\theta+\chi)|$ . The combination depends on the wafer orientation and the type of bending. For example, the optimal multi-wafer configuration is presented in Fig. 10 for a cylindrically bent plate of [100] orientation. Using the optimal combination between  $\theta$  and  $\chi$  the slope of the phase space window was calculated in Fig. 11. A few phase space diagrams are given in Fig. 12. The change of  $\theta$  involves a rotation of the phase space window in the  $(\gamma, \Delta k/k)$  plane. The size of the window is determined by the maximum angle accepted by the BM ( $l^{max}/L_0$ ). The relative window size for both angle and wavelength is shown in Figs. 13 and 14. Assuming a maximum acceptance angle of  $10^\circ$  ( $l^{max}/L_0 = 0.175$ ), a wavelength window of 4% is achievable for  $\theta$  in the range from  $20^\circ$  to  $50^\circ$  with an angular acceptance in the  $1^\circ$ - $3^\circ$  range.

In combination with TOF, Bragg mirrors make it possible to record a single diffraction line or a few close lines along with their higher orders. Each diffraction line will provide a mapping of the sample. Two-dimensional mapping (of crystal phases, texture or strains) is done in a single measurement at the spatial resolution of the Bragg mirror and the wavevector transfer resolution in diffraction by the TOF method. This opens entirely new opportunities in materials studies. For imaging by elastic scattering, Bragg mirrors with asymmetric reflection  $\chi \neq 0$  are the

best solution. The wavelength acceptance window can be widened (up to 10%). However, at a given wavelength the angular acceptance will be then reduced (down to 1° per centimeter of crystal thickness).

To increase the wavelength acceptance window the BM can be rotated synchronously with the neutron pulse. The acceptance diagrams will then move in the  $(\gamma_0, \Delta k_0/k)$  plane following the variation of the Bragg angle on rotation. In this way a BM can be made to reflect a large TOF spectrum of neutrons. The aberration of the sample image recorded by a PSD can no longer be canceled exactly because  $\theta$  has become variable, but the Doppler effect can be exploited for compensation. A small value of  $\chi$  will ensure a larger angular acceptance (i.e., several degrees).

## 6.2. Time-of-flight resolution

The time-of-flight is related to the wavevector transfer in the case of powder diffraction or with the energy transfer in the case of inelastic scattering. These two cases are considered below.

For diffraction, the window of the “elastic” peak will be wide (determined by the wavelength acceptance window of the Bragg mirror) and only the diffraction lines generated by neutron elastic scattering on sample will be registered in this window. In the case of elastic scattering the neutron velocity is constant along the flight path and the BM contribution to the time-of-flight uncertainty is given by the variation of the path induced by the position of the point where reflection occurs. If one considers a diffraction line, there is a correlation between the neutron speed and direction after scattering by the sample. By taking into account this correlation on calculating the point where reflection occurs inside the BM, the following expression is obtained for the BM time-of-flight contribution:

$$\begin{aligned} \left(\frac{\Delta t}{T}\right)_{BM} &= \frac{\cot \theta \cos(\theta + \chi) \cos(\theta - \chi)}{\sin(\theta + \chi) \cos(\theta - \chi) - a \sin 2\chi} \times \frac{g_M}{R_e \operatorname{sgn}(\theta + \chi)} \\ &+ \left[ \cos \chi - \sin \chi \frac{(1 - 2a) \cos(\theta + \chi) \cos(\theta - \chi)}{\sin(\theta + \chi) \cos(\theta + \chi) - a \sin 2\chi} \right] \times \frac{2g_M \sin \theta}{L_S + L_0 + L_1} \end{aligned} \quad (37)$$

where  $a = -\tan \theta_S / \tan \theta$  is the usual dispersion parameter. In principle this contribution can be canceled. Then the time of flight focusing occurs. The relation between  $\theta_S$  and  $\theta$  at time of flight focusing is calculated in Fig. 15 for the optimal reflectivity configuration previously given in

Fig. 10 and for different ratios between the first flight path ( $L_S$ ) and the distance from sample to BM ( $L_0$ ). Data of such type of can help in assessing BM configurations for diffraction.

For inelastic scattering, a BM is simultaneously a monochromator and an imaging mirror. The energy transfer resolution will include the BM energy resolution and the BM time-of-flight contribution similar to the case of elastic scattering. In this case  $\chi=0$  and the expressions simplify:

$$\left(\frac{\Delta\lambda}{\lambda}\right)_{BM} = \cot^2 \theta \times \frac{g_M}{R_e} \quad (38)$$

$$\left(\frac{\Delta t}{T}\right)_{BM} = \frac{L_0 + L_1}{L_0 + L_1 + \frac{\lambda_i}{\lambda_f} L_S} \times \frac{g_M}{R_e \sin^2 \theta} \quad (39)$$

Overall time-of-flight resolution values below 2% are expected.

## 7. Discussion

### 7.1. Alternative to Bragg Mirror

Alternative methods for microbeam-forming are used in synchrotron radiation (SR) research [24]. Such methods can be useful for imaging in neutron scattering. Some are more promising than others are.

- *Pinhole camera* - This method visualizes the sample on a PSD through a pinhole. The method is aberration free and totally non-dispersive, but the angular acceptance is very low (fraction  $\sim 10^{-6}$  from BM angular acceptance).
- *Total reflecting mirrors* - Ellipsoidal and Kirkpatrick-Baez mirrors have been used in SR focusing arrangements. For this type of arrangement the angular acceptance is also low, being determined by the critical angle in the equatorial plane. Using multilayer mirrors can increase the angular range of specular reflection. In fact these mirrors are a sort of BM with a large d-spacing and a d-spacing gradient through the thickness. For cold neutrons ( $\lambda > 4\text{\AA}$ ) the performance of a multilayer toroidal mirror should be similar to that of a BM based on single crystals.
- *Refractive lens* – It seems sensible that refractive technique [25] are only applicable to very cold neutrons and the influence of gravity complicates the lens design. For cold neutrons

simply adding a large number of non-absorbing lenses can increase the refraction effect [26], but the technical possibility to build large aperture optical devices based on refraction has not been demonstrated.

- *Diffraction lens* - In SR microscopy zone plates and Bragg-Fresnel optics are widely used [24]. The use of such high precision devices is limited to high brilliance radiation source. They provide a submicron image resolution, but the lens dimensions have also to very small (sub-millimeter). Demonstration of such devices in neutron scattering is likely a long way off.

### 7.2. *Materials Science Impact*

The instruments currently used in neutron scattering only provide data averaged over the sampling volume (sometimes called “gauge volume”). The “Bragg mirror” system will provide a high spatial resolution image of neutron scattering from inside the specimen nondestructive. Although the instrument resolution in energy (or  $\Delta Q/Q$  in diffraction) will be moderate, the exceptional spatial distribution data can help materials scientists to accomplish novel solid state and materials science studies including:

- Real-time microstructure analysis of the deformation of materials under static or dynamic load (mapping peak positions & widths);
- Real-time study of phase transformations induced by diffusion or solid state reactions (integrated intensity of selected diffraction lines *versus* time and position in sample);
- High resolution internal strain mapping (peak positions & integrated intensities);
- Stroboscopic examination of periodic motions in materials (Doppler shift of diffraction lines);
- *In-situ* observation of the diffusion of water or hydrocarbons in materials by inelastic neutron scattering (intensity of selected inelastic scattering lines *versus* time and position in sample);
- Dynamic structure factors and frequency distributions in inhomogeneous samples (mapping inelastic scattering intensity as function of T, P, H, etc.).

### 7.3. *Estimates*

At a modest spatial resolution of 1 mm the BM can deliver to a PSD a two-dimensional image of over 500 points. For diffraction an angular acceptance of  $3 \times 10^{-3}$  sterad is achievable. One BM at a pulsed source is equivalent from the point of view of data collection speed to a detection

system covering 1/8 of the full sphere around the sample and collecting data from a single point of the sample. A BM peak reflectivity of 50% and only one diffraction peak of interest were assumed. The basic limitation of the BM use is the small wavelength window (~ 4%). An increase up to 20% can be obtained by rotating the BM synchronously with the neutron pulse.

The authors are grateful to Dr. Stephen Spooner and Dr. David Wang for help in the demonstration experiment. Research sponsored by the Assistant Secretary for Energy Efficiency and Renewable Energy, Office of Transportation Technologies, as part of the High Temperature Materials Laboratory User Program, Oak Ridge National Laboratory, managed by UT-Battelle, LLC, for the U.S. Department of Energy under contract number DE-AC05-00OR22725. The U.S. Department of Energy also supported in part one of the authors (MP) through contract DE-FG02-96ER45599.



## Notation summary

$A, B$ : material constants describing the elastic deformation of the crystal in the thin plate approximation;

$a$ : dispersion parameter  $a = -\tan\theta_s/\tan\theta$ ;

$a_{ij}$ : elements of matrix relating the lattice distortion inside the with the scattering location in the crystal coordinate system [see relation (7)];

$A_{ijk}, B_{ijk}$ : general aberration coefficients [see relation (34)];

$b_{ij}$ : elements of matrix relating the lattice distortion inside the crystal with the scattering location in the neutron beam coordinate system [see relation (9)];

$C_{ij}$ : reflection matrix elements [see relation (10)];

$$c_+ = \frac{\cos(\theta + \chi)}{\sin 2\theta}; c_- = \frac{\cos(\theta - \chi)}{\sin 2\theta}; s_+ = \frac{\sin(\theta + \chi)}{\sin 2\theta}; s_- = \frac{\sin(\theta - \chi)}{\sin 2\theta};$$

$\frac{\Delta k_0}{k}, \frac{\Delta k_1}{k}$ : relative deviations of wavevector modulus of current neutron before and after

diffraction on bent perfect crystal;

$\frac{\Delta\lambda}{\lambda}$ : relative wavelength deviation;

$\left(\frac{\Delta\lambda}{\lambda}\right)_{\max}$ : relative wavelength window;

$\frac{\Delta t}{T}$ : relative time-of-flight deviation;

$\frac{\Delta\tau_1}{\tau}, \frac{\Delta\tau_2}{\tau}$ : relative deviations of current reciprocal-lattice vector along  $\tau_0$  and perpendicular to it

in the diffraction plane;

$f$ : characteristic distances defined for elastic bending [relation (18')] used to calculate the reflection matrix elements and the phase space acceptance window [see relations (18) and (19)];

$f_0, f_1$ : first and second focal lengths (before and after diffraction, respectively), relation (2);

$f_a$ : focal length in the axial (sagittal) plane, relation (31);

$g_M, l_M, z_M$ : coordinates in the crystal (thickness, lateral extent and height);

$g_M^{\max}, l_M^{\max}, z_M^{\max}$ : crystal dimensions (thickness, lateral extent and height);

$\gamma_0, \delta_0$ : angular deviations of incoming neutron, in the diffraction plane and out of diffraction plane;

$\gamma_l, \delta_l$ : angular deviations of scattered neutron;  
 $L_0, L_l$ : distances from source to crystal and from crystal to image, respectively;  
 $L_0^*, L_l^*$ : optimal distances for imaging in the ideal bending case [see relation (20') and (30a)];  
 $L_S$ : distance from neutron moderator to sample in the time-of-flight arrangement;  
 $M$ : magnification, defined in general by relation (33);  
 $\theta, \chi$ : crystal Bragg and cutting angles, respectively ( $\chi = 0$  for symmetric reflection);  
 $\theta_S$ : scattering angle of the sample; the detector angle in diffraction is  $2\theta_S$ ;  
 $R_e, R_a$ : crystal radius of curvature in the equatorial and axial planes, respectively;  
 $\tau_0$ : reciprocal-lattice vector of the unbent crystal;  
 $v_n$ : neutron velocity;  
 $y_0, z_0$ : neutron coordinates across the incoming beam;  
 $y_l, z_l$ : neutron coordinates across the diffracted beam.

## References

1. Egert, G. & Dachs, H. (1970). *J. Appl. Cryst.*, **3**, 214-220.
2. Popovici, M., Stoica, A. D. & Ionita, I. (1987). *J. Appl. Cryst.*, **20**, 90-101.
3. Stoica, A. D. & Popovici, M. (1989). *J. Appl. Cryst.* **22**, 448-454.
4. Popovici, M., Yelon, W. B., Berliner, R., Stoica A. D., Ionita, I., & Law, R. (1994). *Nucl. Instrum. Methods*, **A 338**, 99-110.
5. Popovici, M., Yelon, W. B., Berliner, R. & Stoica, A. D. (1997), *Proceedings of the Workshop on Neutron Scattering Instrument Design, Berkeley, 1996*, edited by R. P. Hjelm, Report LBNL-40816, pp. 55-61.
6. Wagner, V., Mikula, P. & Lukas, P. (1994). *Nucl. Instrum. Methods*, **A 338**, 53-59.
7. Popovici, M. & Yelon, W. B. (1995). *J. Neutron Res.*, **3**, 1-25.
8. Popovici, M. & Yelon, W. B. (1997). *J. Neutron Res.*, **5**, 227-239.
9. Yelon, W. B., Berliner R. & Popovici, M. (1998). *Physica*, **B 241-243**, 237-239.
10. Stoica, A. D., Popovici, M. & Yelon, W. B. (2000). *J. Appl. Cryst.* **33**, 137-146.
11. Kulda, J., Wagner, V., Mikula, P. & Saroun, J. (1994). *Nucl. Instrum. Methods*, **A 338**, 60-64.
12. Kulda, J. & Saroun, J. (1996). *Nucl. Instrum. Methods*, **A 379**, 155-166.
13. Rekveldt, M.Th. (1983). *Nucl. Instrum. Methods*, **215**, 521-527.
14. Arrott, A. S. & Templeton, T. L. (1985). *J. Appl. Cryst.*, **18**, 388-395.
15. Stoica, A. D., Popovici, M., Yelon, W. B. & Berliner, R. (2000). *J. Appl. Cryst.* **33**, 147-155.
16. Stoica, A. D., Popovici, M., Hubbard, C. R. & Spooner, S. (1999). *ORNL/TM1999/277*.
17. Stoica, A. D., Popovici, M., Spooner, S. & Hubbard, C. R. (2000). *ICRS-6, Proceedings of The 6-th International Conference on Residual Stress*, Oxford, UK, 1255-1263.
18. Stoica, A. D., Popovici, M. & Hubbard, C. R. (2000). Submitted to *J. Appl. Cryst.*
19. Lukas, P. & Kulda, J. (1989). *Phys. Stat. Sol.*, **B156**, 41-48.
20. Kulda, J. (1984). *Acta Cryst.*, **A 40**, 120-126.
21. Popovici, M. & Stoica, A. D. (1983). *J. Phys. E: Sci. Instr.*, **16**, 662-665.
22. Copley, J. R. D. (1993). *J. Neutron Res.*, **1**, 21-36.
23. Stoica, A. D., Popovici, M. & Yelon, W. B. (1999). *J. Appl. Cryst.* **32**, 744-754.
24. Ice, G. E. (1997). *X-Ray Spectrometry*, **26**, 315-326.
25. Lengeler, B., Schroer, C., Tuemmler, J., Snigirev, A. A., Snigireva I. & Drakopoulos, M. (1999). *SPIE Conference 3737, "EUV, X-Ray, and Neutron Optics and Sources"*, Denver.
26. Bishop, D. J. (1999). *SPIE Conference 3737, "EUV, X-Ray, and Neutron Optics and Sources"*, Denver.

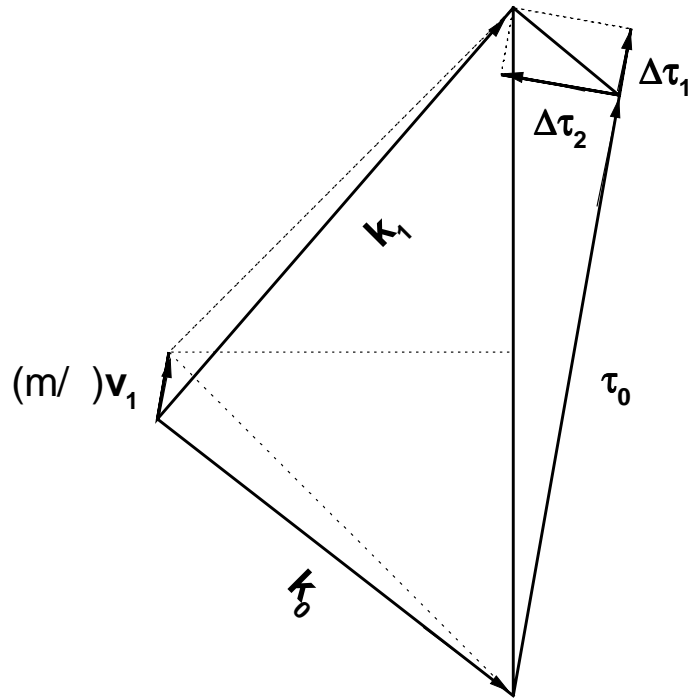


**Fig. 1** Geometry of the diffraction process in reciprocal space.

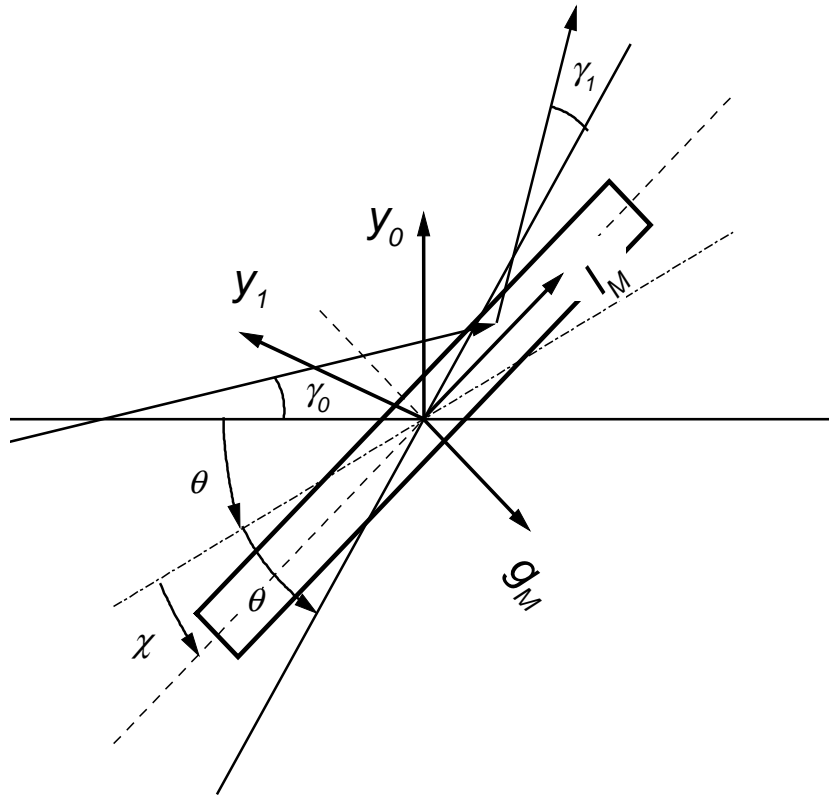


**Fig. 2** Geometry of the diffraction process in real space.

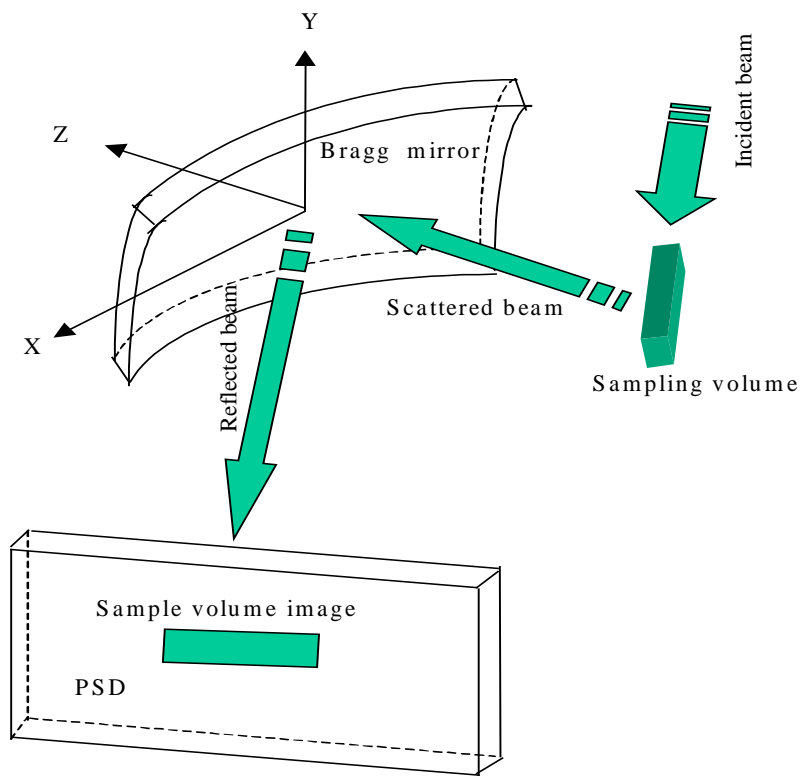


**Fig. 3** Schematic of the BM imaging system. Each pixel in the PSD provides scattering information corresponding to a specific location in the sample.



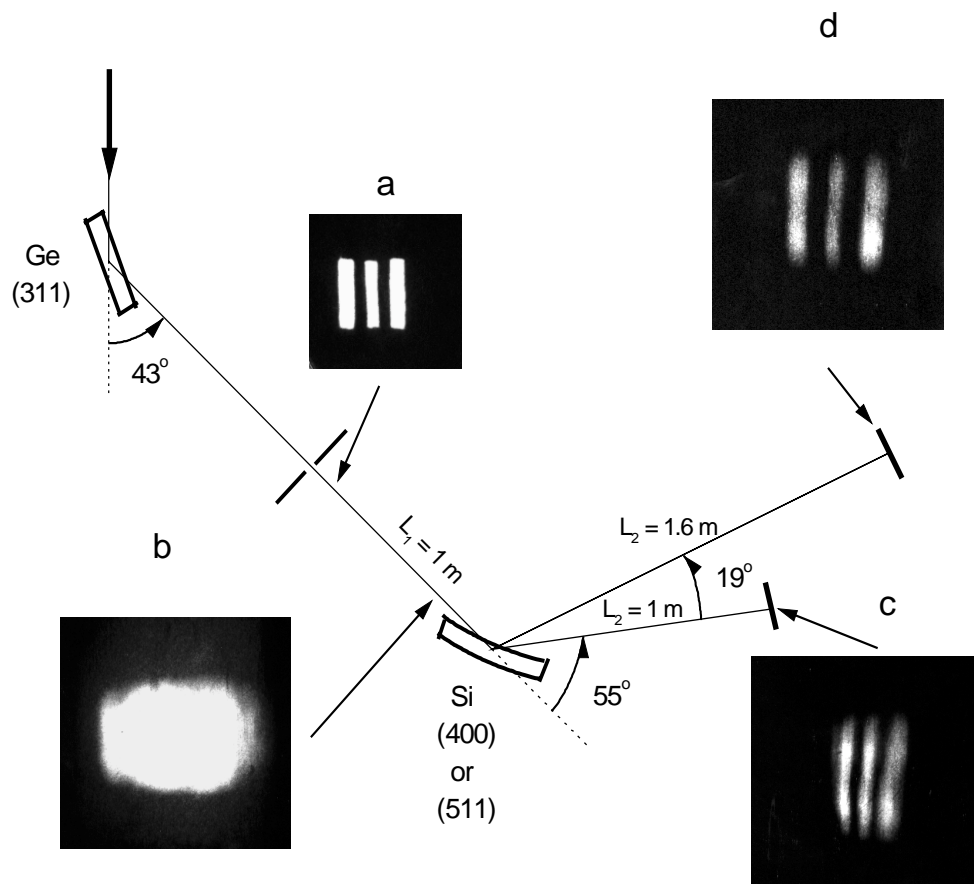
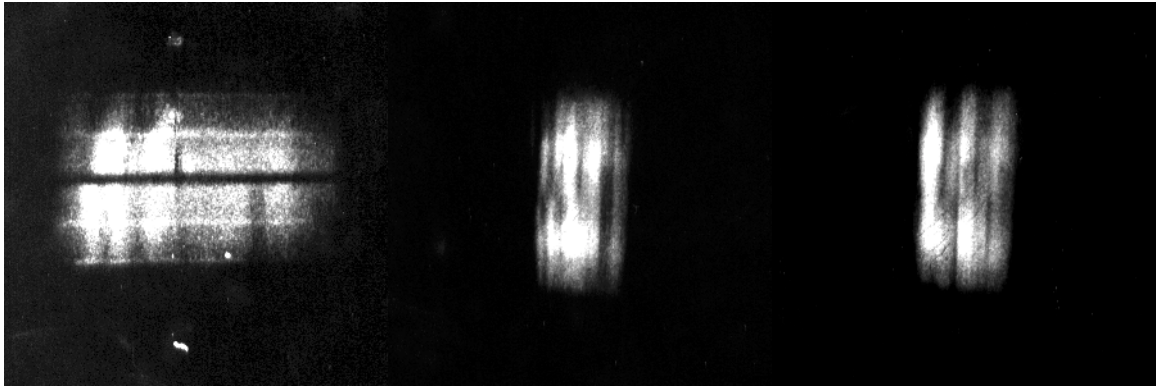


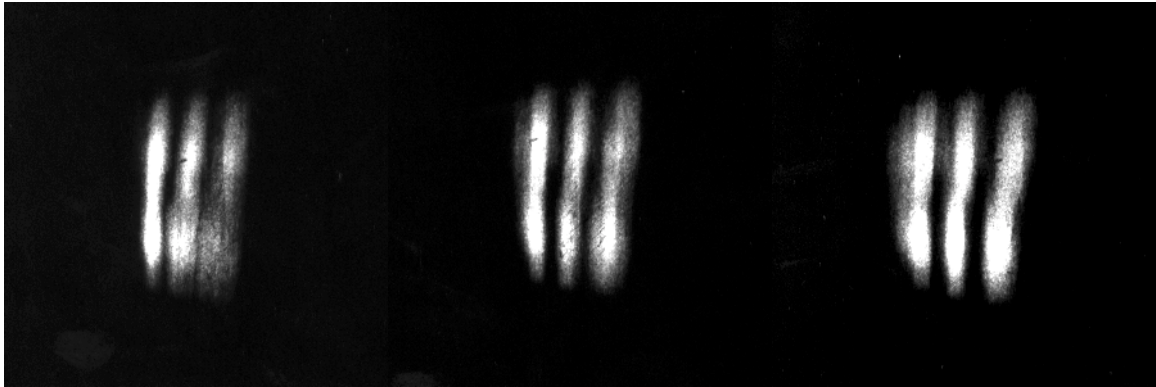
**Fig. 5** Bragg Mirror demonstration experiment. a) – neutron beam after slits; b) – neutron beam before Bragg Mirror; c) – image of the slits for  $M = 1$ ; d) – image of the slits for  $M = 1.5$  .



$L_2 \sim 15$  cm

$L_2 = 80$  cm

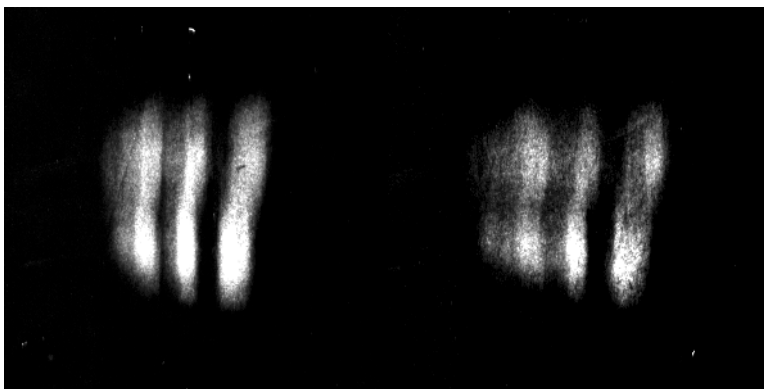
$L_2 = 90$  cm



$L_2 = 95$  cm

$L_2 = 100$  cm

$L_2 = 105$  cm



$L_2 = 110$  cm

$L_2 = 120$  cm

**Fig. 6** Image formation: beam profile at different distances after BM.  $L_1 \sim 100$  cm and  $R_e \sim 230$  cm.



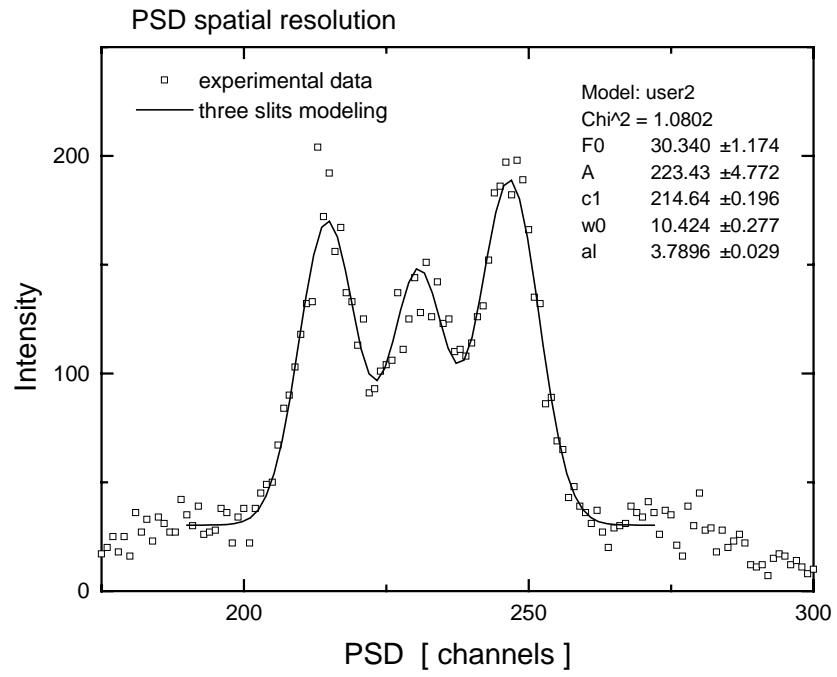


**Fig. 7**

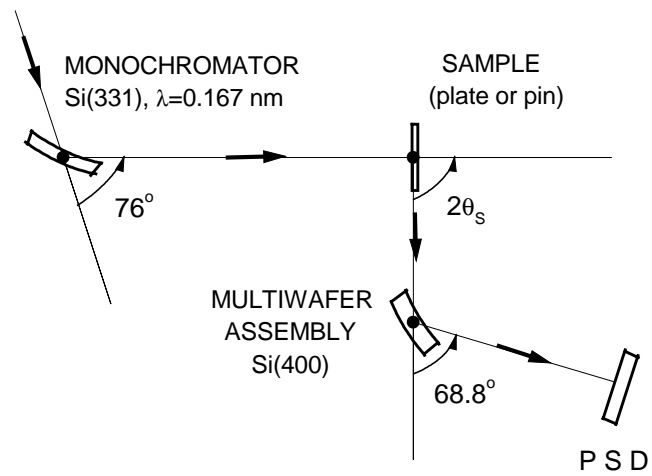


**Fig. 8**

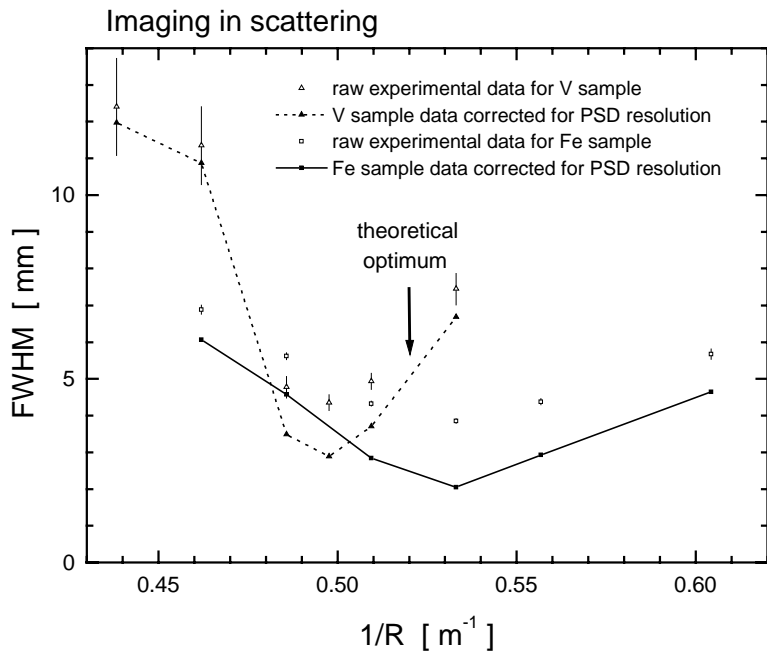


**Fig. 9**

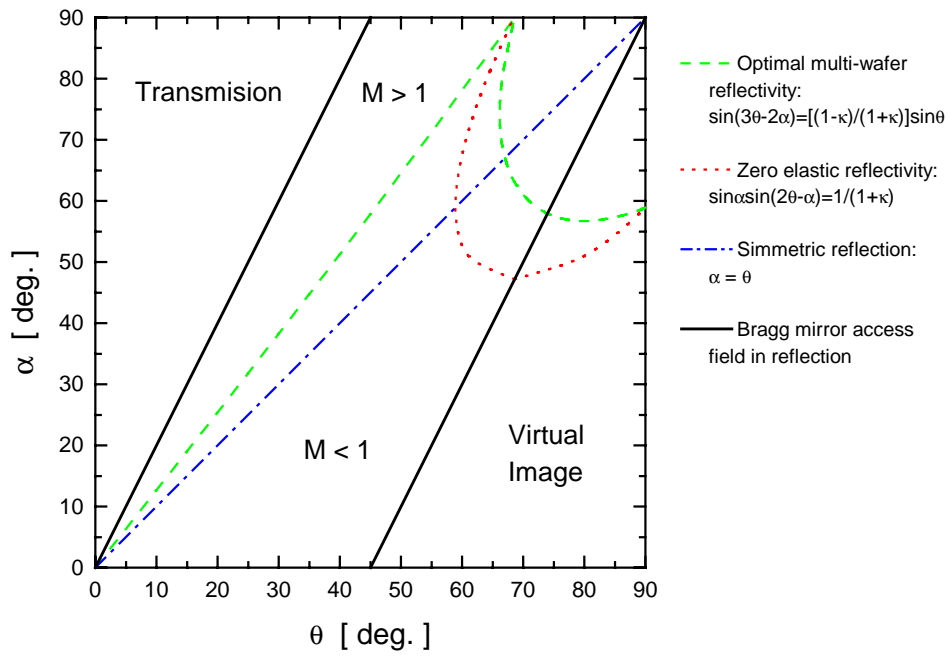


**Fig. 10**

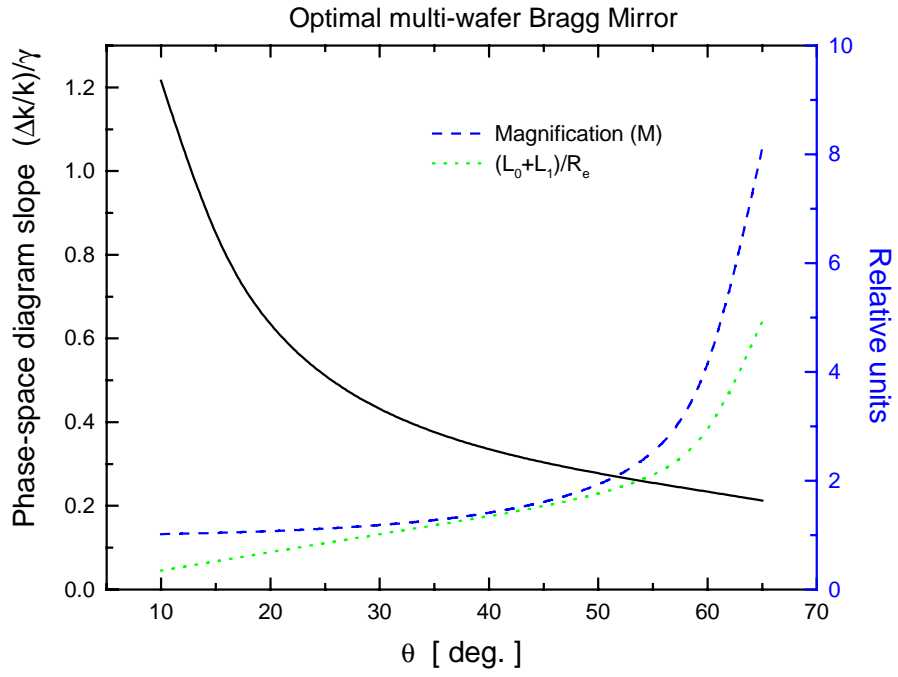


Fig. 11

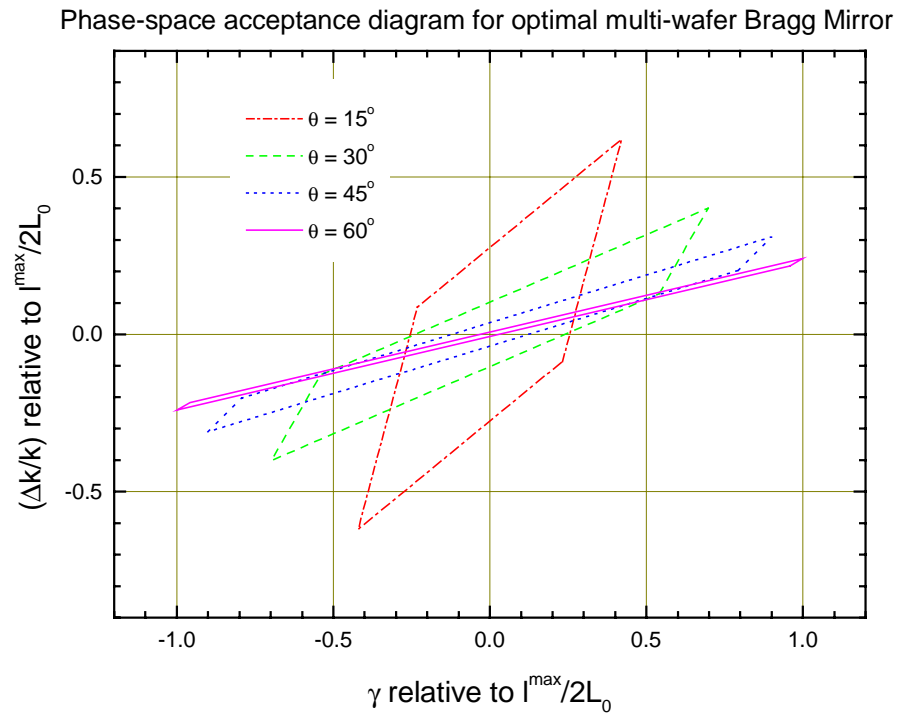


Fig. 12

Phase-space acceptance window for optimal multi-wafer Bragg Mirror

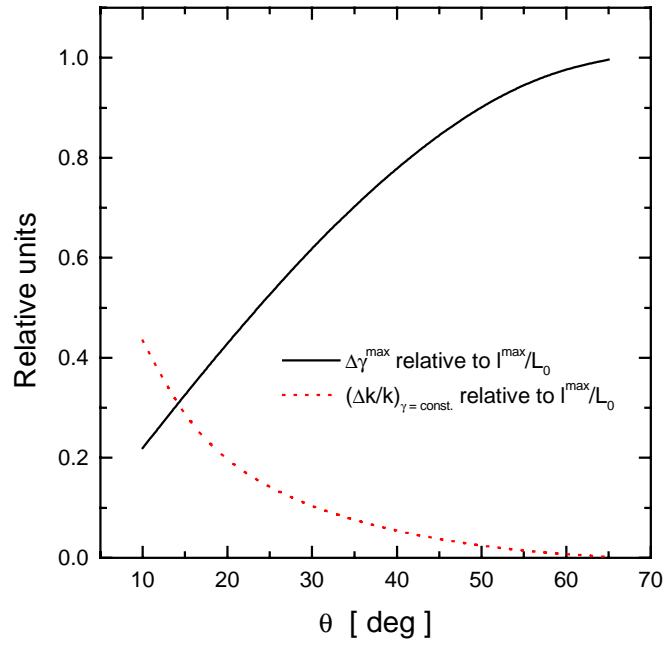


Fig. 13

Phase-space acceptance window for optimal multi-wafer Bragg Mirror

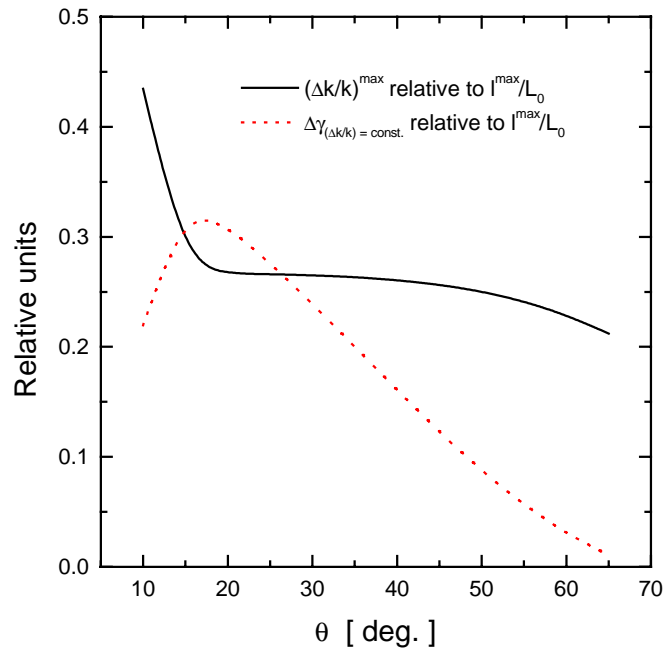
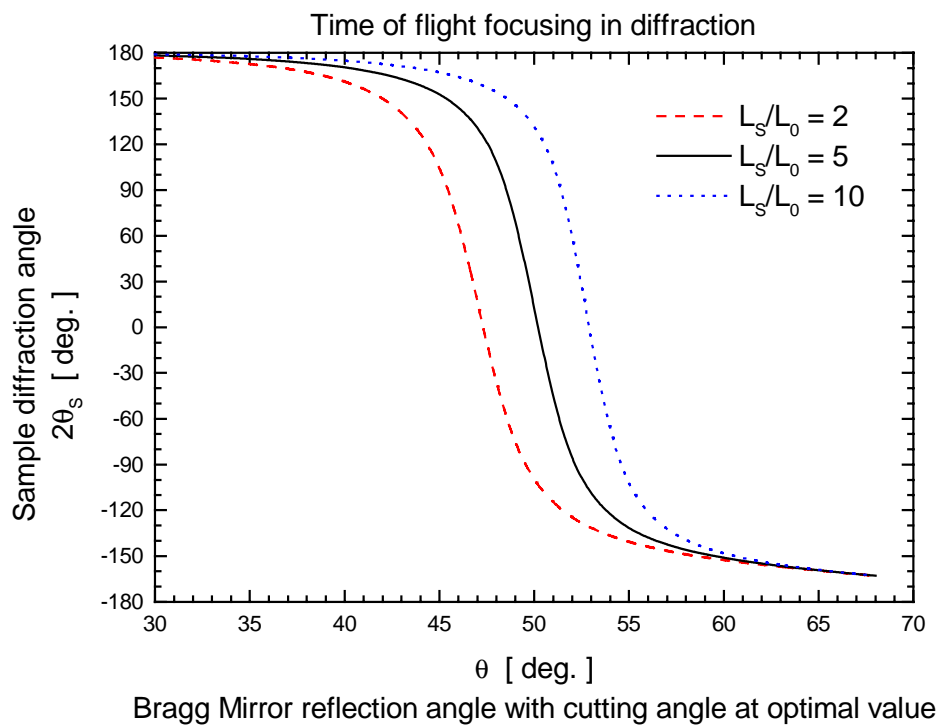


Fig. 14



**Fig. 15**